RSC Advances

PAPER

View Article Online
View Journal | View Issue

Cite this: *RSC Adv.*, 2025, **15**, 29613

Proton-coupled pseudocapacitive behavior of a manganese oxide-decorated nitrogen-rich COP for sustainable high-performance energy storage devices

Nakul Desai,[a] Y. N. Sudhakar,*[a] M. Selvakumar[a] and Dheeraj Devadiga[b]

A hierarchical hybrid material (Mn_2O_3@COP) with dual charge storage capabilities was created by synthesizing a triazine-based covalent organic polymer (COP) that is rich in nitrogen functionalities and integrating it with Mn_2O_3 nanoparticles. Fourier transform infrared spectroscopy (FTIR), X-ray diffraction (XRD), scanning electron microscopy (SEM), energy dispersive X-ray spectroscopy (EDS), Brunauer–Emmett–Teller (BET) studies, and X-ray photoelectron spectroscopy (XPS) demonstrated a distinct architecture: Mn_2O_3 nanoparticles were uniformly embedded in a stable, porous COP matrix. Mn_2O_3 loading caused a modest decrease in surface area, but the composite still had the mesoporosity needed for quick ion diffusion. The existence of electroactive nitrogen centers—pyridinic, pyrrolic, and graphitic—and mixed-valence Mn^{3+}/Mn^{4+} species, which together improve redox kinetics and charge transfer routes, was verified by XPS analysis. An intriguing combination of electric double-layer capacitance (EDLC) and pseudocapacitive behavior was demonstrated by electrochemical experiments in a 1 M H_2SO_4 electrolyte. The Mn_2O_3@COP composite electrode in the three-electrode system had a high specific capacitance of 113 F g^{-1} at 5 mV s^{-1} and 69.1 F g^{-1} at 0.1 A g^{-1}, an energy density of 9.6 Wh kg^{-1} and a power density of 500 W kg^{-1} at 0.1 A g^{-1}. The fabricated symmetric supercapacitor device maintained 95% of its capacitance after 10 000 charge–discharge cycles at 0.5 A g^{-1} and provided a specific capacitance of 16.2 F g^{-1} and energy density and power density of 2.25 Wh kg^{-1} and 250 W kg^{-1} at 0.2 A g^{-1}, respectively. This study offers a viable method for combining the energy density of transition metal oxides with the quick kinetics of conductive organic networks, opening the door to long-lasting, highly effective energy storage devices.

Received 8th July 2025
Accepted 14th August 2025

DOI: 10.1039/d5ra04868k

rsc.li/rsc-advances

1 Introduction

The rapid rise in population has led to a significant surge in energy demand across all sectors—from everyday necessities to large-scale industrial operations. Currently, fossil fuels such as coal, natural gas, and oil are major contributors, accounting for nearly one-third of global greenhouse gas emissions. In the 21st century, one of the most critical challenges is ensuring access to cleaner, more reliable energy while simultaneously improving quality of life. This highlights the pressing need to transition toward sustainable, renewable, and eco-friendly energy alternatives. Renewable sources such as solar and wind power offer viable alternatives to the crisis of fossil fuels, and their intermittent nature presents challenges for grid integration. However, to guarantee a steady supply of energy, their intermittent output calls for the creation of advanced energy storage technologies.[1] Various energy storage technologies, such as batteries and supercapacitors, have emerged as key solutions to address these challenges of the global energy crisis.[2] They bridge the gap between the demand and supply of energy. Since 1995, batteries have emerged as among the greatest energy storage devices that provide high energy density outputs. However, despite their high energy density, they possess low power density, which is their major drawback. In addition to batteries, supercapacitors are advantageous because of their high-power density, rapid charge/discharge rates, and long cycle life, making them ideal for applications such as regenerative breaking, grid stabilization, and backup power.[3] Supercapacitors come into play when practical applications call for an energy storage device that can offer the advantages of high energy density and significant power density. They bridge the gap between capacitors and batteries. The electrode is a major part of the supercapacitor and determines the performance of the supercapacitor. Hence, the choice of electrode material plays a crucial role in the performance of a supercapacitor.

[a]*Department of Chemistry, Manipal Institute of Technology, Manipal Academy of Higher Education, Manipal-576104, India. E-mail: sudhakar.yn@manipal.edu*
[b]*Manipal Technologies Limited, Manipal, 576104, Karnataka, India*

A wide range of materials have been explored for supercapacitor applications, and mainly carbon-based materials (activated carbon, carbon nanotubes, graphene, mesoporous carbon, *etc.*), metal oxides and hydroxides, conducting polymers, and composite materials have been extensively studied. These materials often face limitations such as low energy density, limited specific capacity, and mechanical instability. Composite materials, however, offer a promising alternative by synergistically enhancing conductivity, stability, and capacitance, making them highly effective for next-generation supercapacitors.[4] Several articles highlighting the above-mentioned materials have been published. Hou *et al.* reported a hierarchically nanostructured polypyrrole/MXene hybrid hydrogel modified with a lignosulfonate composite as an electrode material for supercapacitor applications. Even though the symmetric device has an energy density of 29.3 Wh kg^{-1} and a power density of 3200 W kg^{-1}, it faces several challenges, such as aggregation and restacking of the MXene layers, poor mechanical and structural stability of the polypyrrol, and interface control and optimization of the hybrid composition.[5] Similarly, an Ag@TiO_2 nanotube array composite was used as an anode material for sodium metal battery applications. The device achieved 87% capacity retention after 2000 cycles at 8 C. However, the composite has the major drawback of dendrite formation in sodium metal.[6] Another report described a Cu-MoO_3 composite as an anode material for a zinc-ion battery. The composite showed a capacity of 254.4 mAh g^{-1} at 0.4 A g^{-1}. The composite has the major drawback of precisely tuning the Cu concentration to generate an optimal oxygen vacancy density without compromising structural integrity or introducing unwanted phases, which affect the performance of the device.[7]

Despite these composite materials and their drawbacks, covalent organic polymers (COPs) have emerged as promising electrode materials for supercapacitors because of their exceptional chemical and structural properties. As a subclass of crystalline and porous covalent organic frameworks (COFs), COPs consist of organic molecules linked by covalent bonds, offering a highly tunable platform for energy storage applications. Unlike traditional inorganic materials, COPs provide extensive chemical versatility, enabling precise control over their electronic, electrochemical, and structural characteristics. These properties make COPs highly suitable for efficient energy storage, as they have a high surface area, tunable porosity, and excellent structural stability. The ability of these materials to function with redox-active groups further enhances their pseudocapacitive charge storage capabilities, significantly improving the overall energy density of asymmetric supercapacitors. Additionally, their inherent stability and excellent rate capability ensure long-term cycling performance, making them a compelling choice for next-generation energy storage devices.[8] Tao *et al.* reported the use of nickel-doped COF (Ni-COF) as an electrode material for an asymmetric supercapacitor; the device exhibited an excellent specific capacitance of 417 F g^{-1} at 1 A g^{-1} and high energy and power densities of 130 Wh kg^{-1} and 839 W kg^{-1}, respectively.[9] Kang *et al.* developed an antimony-doped triphenyl stibine-based COF (Sb-COF) composite as an electrode material for asymmetric supercapacitors. The device showed an excellent specific capacity of 78.6 F g^{-1} at 3 A g^{-1} with an energy density of 44 Wh kg^{-1} and a power density of 3024 W kg^{-1}.[10]

On the other hand, metal oxides have emerged as promising electrode materials for high-performance supercapacitors owing to their remarkable specific capacitance, favorable electrical conductivity, and superior electrochemical stability. Typically, these materials exhibit higher charge storage capacities per unit mass or volume than other electrode candidates do.[11] Prominent examples of metal oxides utilized in energy storage applications include manganese(III) oxide (Mn_2O_3), manganese dioxide (MnO_2), nickel oxide (NiO), cobalt oxide (Co_3O_4), ruthenium dioxide (RuO_2), vanadium pentoxide (V_2O_5), titanium dioxide (TiO_2), molybdenum trioxide (MoO_3), *etc.* In comparison, Mn-based oxides have garnered much attention because of their affordability, availability, and environmental friendliness. Mn_2O_3 has shown great promise as an electrode material for supercapacitor applications. Many studies have investigated the outstanding physicochemical properties of Mn_2O_3, making it a suitable candidate for electrode applications. Ansari *et al.* reported the synthesis of porous hollow double-walled Mn_2O_3 nanocubes through a hydrothermal approach, which demonstrated a high specific capacitance of 256.25 F g^{-1} along with excellent cyclic stability, retaining 90% of the initial capacitance after 3000 charge–discharge cycles.[12] Li *et al.* synthesized porous Mn_2O_3 nanocubes *via* a hydrothermal method, achieving a specific capacitance of 191.1 F g^{-1} at a current density of 0.1 A g^{-1}, along with a rate capability of 58.6%.[13] Similarly, Xu *et al.* fabricated porous Mn_2O_3 microsheet arrays, which exhibited a high specific capacitance of 566.6 F g^{-1} at 0.5 A g^{-1}, which decreased to 294.4 F g^{-1} when the current density was increased to 20 A g^{-1}, indicating good rate performance.[14] Although Mn_2O_3 has been extensively investigated, there is still a great deal of unrealized potential to increase its capacity and energy storage capacity by means of structural modification, doping strategies, composite formations, *etc.*[15] Recent studies on Prussian blue analogues (PBAs) for sodium-ion storage emphasize the value of combining transition-metal redox activity with robust, ion-accessible frameworks to boost energy and power densities. Yet, PBAs face issues such as structural degradation, vacancy instability, and sluggish ion transport, addressed through strategies like particle size control, surface functionalization, and framework integration.[16] These principles extend to Mn_2O_3 systems, where incorporating it into a conductive, porous COP matrix can enhance redox accessibility, stabilize morphology, improve electrolyte interaction, and overcome ion diffusion barriers for superior capacitive performance. Tong *et al.* observed in recent battery management studies, electrochemical performance is often limited by material degradation, including capacity loss, increased resistance, and polarization changes during cycling.[17] Such challenges underscore the importance of frameworks that combine active redox materials with robust structural matrices. In this context, embedding Mn_2O_3 within a covalent organic polymer (COP) offers a pathway to maintain high capacitance, mitigate structural degradation, and ensure stable operation in long-term energy storage applications. Many other recent

advances in energy storage highlight the need for electrode materials that combine high performance with long-term stability.[18] In lithium-ion systems, hybrid model- and data-driven approaches have improved performance retention under aging, while optimized structural designs in thermal management have enhanced operational consistency.[19] Translating these principles to material design, embedding Mn_2O_3 within a conductive COP can integrate efficient redox activity with mechanical and structural resilience, offering a robust platform for high-rate capacitive performance and extended cycling life in next-generation hybrid energy storage devices.[20,21]

We report a Mn_2O_3@COP composite, where Mn_2O_3 nanoparticles are uniformly embedded within a nitrogen-rich triazine–urea-linked COP matrix. This hybrid structure offers synergistic integration of faradaic and non-faradaic charge storage mechanisms, facilitating rapid ion diffusion, enhancing conductivity, and improving structural integrity during cycling. Unlike previously reported Mn_2O_3-based composites that suffer from poor cycle life or COP systems with limited capacitance, the Mn_2O_3@COP electrode material demonstrates enhanced electrochemical performance, superior rate capability, and remarkable cycling stability. This work introduces a cost-effective and scalable synthesis strategy for hybrid materials, paving the way for their application in high-performance energy storage devices (Fig. 1).

2 Materials and methods

2.1 Materials

Cyanuric chloride (98.5%), urea (98%), and acetone (99%) were purchased from Loba Chemical. Manganese oxide (99%) was purchased from BLD Pharma. Tetrahydrofuran (99.9%) was purchased from Merck.

2.2 Synthesis of COP

COP was synthesized *via* a previously reported method.[22] Cyanuric chloride (0.02 mol, 3.69 g) and urea (0.03 mol, 1.8 g) were thoroughly mixed on a magnetic stirrer in a 100 mL beaker and gradually heated to 140 °C with continuous stirring until a molten mixture was obtained. The reaction was maintained under these conditions until the evolution of HCl ceased, indicating that upon completion of the reaction, the mixture was cooled to room temperature. The resulting foamy white solid was successively washed with water, tetrahydrofuran (THF), and acetone, followed by vacuum drying, yielding the final product with an overall yield of 76% (Fig. 2).

2.3 Synthesis of the Mn_2O_3@COP composite

COP and Mn_2O_3 were mixed at a weight ratio of 1 : 1 by dispersing them in 30 mL of distilled water and then transferred to a Teflon autoclave vessel. The vessel was placed in a muffle furnace at 150 °C for 16 hours. The resulting dark-colored solid was then filtered and washed thrice with acetone, methanol and multiple rinses with water. Finally, the product was dried, and the obtained product was named the Mn_2O_3@COP composite (Fig. 3).

2.4 Electrochemical characterization and supercapacitor fabrication

Mn_2O_3@COP was used as the active material; it was mixed with polyvinylidene fluoride (PVDF) and *N*-methyl pyrrolidone (NMP) at a ratio of 8 : 1 : 1 to form a uniform slurry. This slurry was coated on a 1 cm × 1 cm dimension stainless steel (SS) sheet, which was used as a working electrode along with Ag/AgCl as a reference and platinum foil as a counter electrode. A swagelok-type cell was constructed with Mn_2O_3@COP as both electrodes

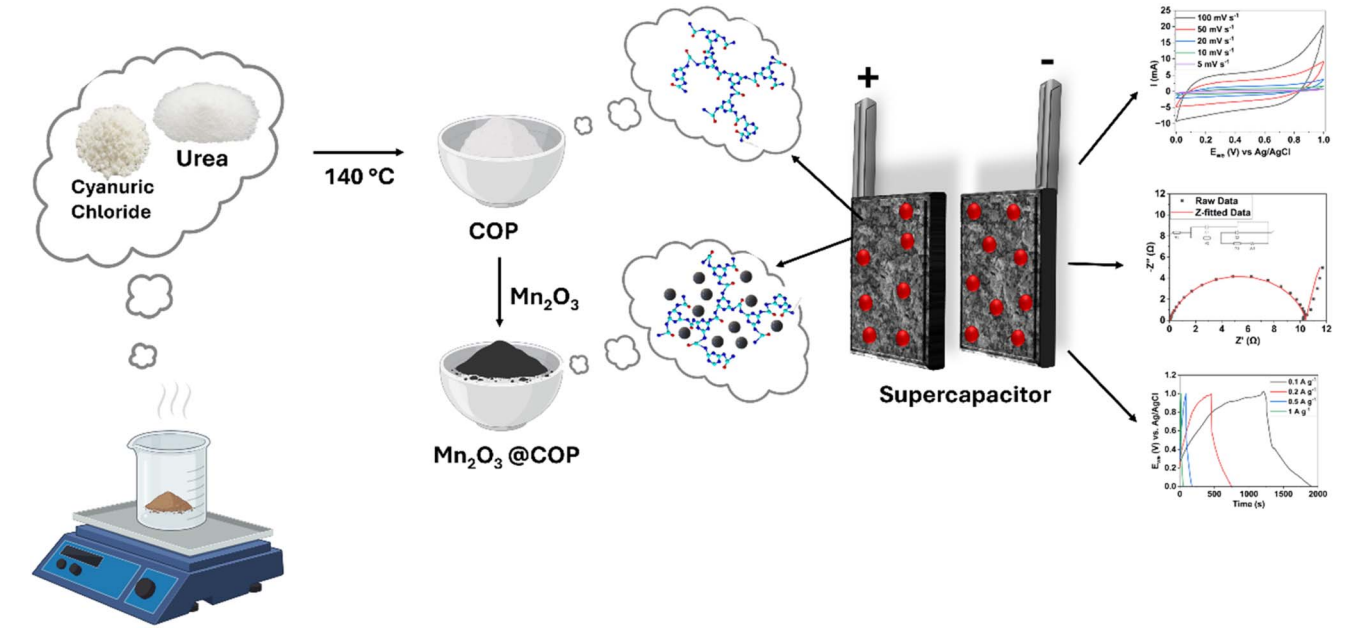

Fig. 1 Graphical abstract of the synthesis, fabrication and electrochemical behavior of the Mn_2O_3@COP composite electrode.

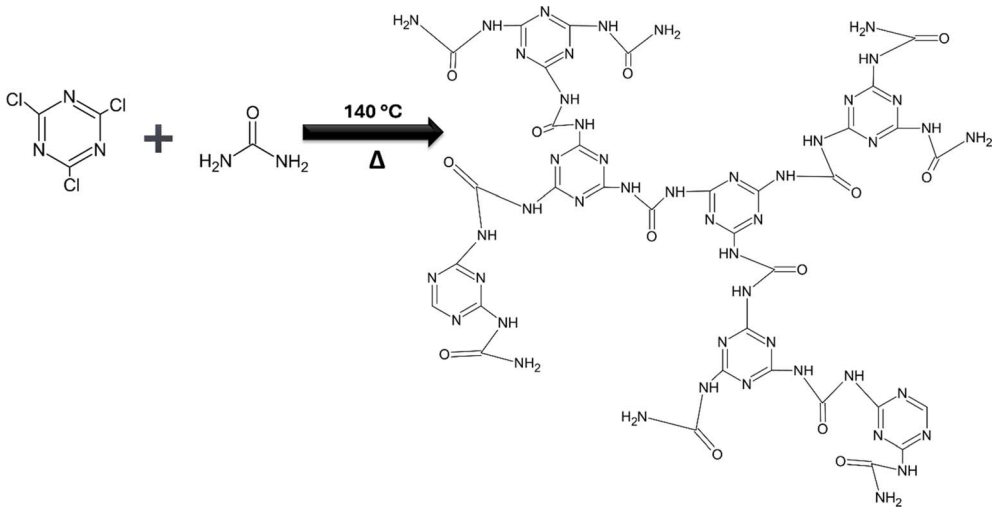

Fig. 2 Schematic representation of the polymerization reaction between cyanuric chloride and urea to synthesize increase the COP.

for the symmetric device (Mn_2O_3@COP//Mn_2O_3@COP). The electrochemical studies for both the three- and two-electrode systems were carried out in a 1 M H_2SO_4 electrolyte solution *via* an electrochemical workstation (Biologic, SP-50e, France).

2.5 Material characterization

The crystallinity of the as-prepared material was analyzed *via* X-ray diffraction (XRD) with a Bruker D8 instrument (Bruker, USA) with a Cu Kα radiation source (40 kV, 40 mA). The chemical interactions in the material were identified *via* Fourier transform infrared (FTIR) spectroscopy (Shimadzu, IRSpirit, Japan). The morphology of the material was determined *via* field emission scanning electron microscopy (Thermo Fisher Scientific and ZEISS, EVO MA18 with Oxford EDS (X-act), IT700 HR). Energy-dispersive X-ray spectroscopy (integrated with FESEM) was used to analyze the elemental composition of the as-prepared material. X-ray photoelectron spectroscopy was carried out *via* a ThermoFisher instrument (Nexsa base, K-α). The surface area was determined *via* Brunauer–Emmett–Teller (BET) analysis (BELSORP mini-X, BELPREP VAC 111, Japan).

3 Results and discussion

3.1 FTIR studies

The FTIR spectra clearly demonstrated the successful synthesis and integration of the Mn_2O_3@COP composite (Fig. 4). In the case of cyanuric chloride, distinct peaks between 700 and 1600 cm^{-1} highlight its triazine ring structure, with a notable

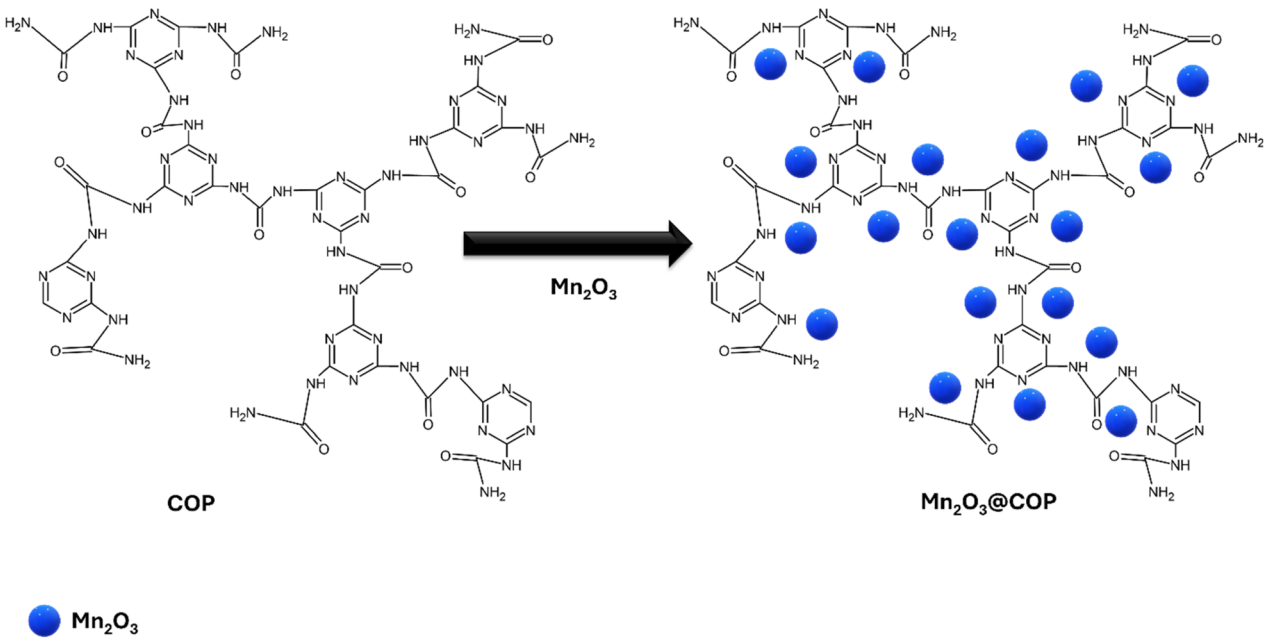

Fig. 3 Schematic illustration showing the incorporation of Mn_2O_3 nanoparticles into the COP matrix.

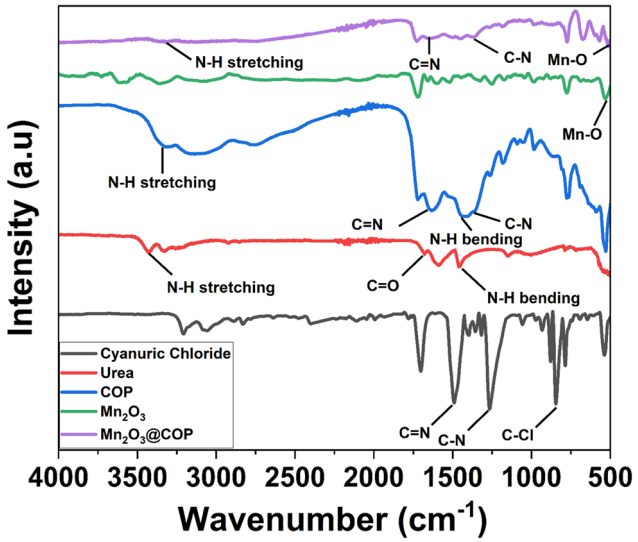

Fig. 4 FTIR spectra of CC, urea, COP, Mn_2O_3, and Mn_2O_3@COP.

peak at approximately 810 cm^{-1} attributed to C–Cl stretching and others between 1350 and 1550 cm^{-1} corresponding to C–N and C=N vibrations.[23] Urea, on the other hand, shows a broad, intense band from 3300 to 3500 cm^{-1} due to N–H stretching, alongside a strong C=O stretching peak at approximately 1670 cm^{-1} and N–H bending modes near 1450–1550 cm^{-1}.[24] Upon polymerization, the FTIR spectrum of the resulting COP undergoes notable changes, indicating the formation of new covalent bonds. The broad absorption at approximately 3300 cm^{-1} suggests the presence of N–H groups, potentially from unreacted amines or trace moisture. A sharp peak near 1625–1650 cm^{-1} confirms the formation of C=N bonds, which is consistent with triazine ring formation through nucleophilic substitution between cyanuric chloride and urea. Additional peaks between 1350 and 1550 cm^{-1} further support the incorporation of nitrogen-containing linkages.[25] Mn_2O_3 shows strong absorption bands in the 500–700 cm^{-1} region, typical of Mn–O stretching vibrations, confirming its oxide nature.[26] For the Mn_2O_3@COP composite, the spectrum reflects features from both components. The broad N–H stretching band and the C=N peak remains visible, indicating that the structural integrity of the COP is maintained. Moreover, the Mn–O bands confirmed that Mn_2O_3 was successfully incorporated into the polymer matrix. Subtle shifts or changes in peak intensity suggest interactions such as hydrogen bonding or weak coordination between the polymer and Mn_2O_3, indicating a well-integrated hybrid structure. Taken together, these spectral features provide strong evidence for the successful formation of both COP and the Mn_2O_3@COP composite.

3.2 XRD studies

Comprehensive structural information about the synthesized materials may be obtained from X-ray diffraction (XRD) patterns (Fig. 5). Pure cyanuric chloride (black trace) has a diffraction pattern with distinct, sharp peaks that show that it is crystalline. The (100), (110), (111), (002), (210), (211), (310), and (320) planes are represented by prominent diffraction peaks at 2θ values of approximately 14.0°, 15.3°, 24.5°, 27.2°, 29.6°, 33.0°, 40.6°, and 49.0°, respectively.[27] The diffraction pattern of the produced COP material (red trace), on the other hand, is much less intense and broader, with a dominant peak at approximately 27°, which corresponds to the (002) plane and is indicative of the π–π stacking of aromatic layers.[28] The broad properties and lack of sharp peaks suggest that the COP material has an amorphous or weak crystalline structure. Since the (211), (222), (400), (332), (440), and (622) planes correspond to the typical reflections at 2θ values of 23.1°, 32.9°, 38.3°, 45.5°, 50.8°, 55.1°, and 65.5°, the diffraction peaks of pure Mn_2O_3 are in good agreement with those of the conventional cubic bixbyite phase (JCPDS no. 41-1442).[29] The Mn_2O_3@COP composite retains the crystalline signature of Mn_2O_3 with intact peak locations during inclusion into the COP matrix, suggesting that the structural integrity of Mn_2O_3 is maintained after encapsulation. The (222) and (400) planes in particular show discernible broadening and a slight reduction in peak intensity, which can be ascribed to the nanoscale dispersion of Mn_2O_3 within the amorphous COP network as well as potential surface interactions or partial encapsulation by the polymeric matrix. Successful hybrid synthesis without disturbing the crystalline phase of Mn_2O_3 is suggested by the emergence of (002) and (110) reflections in the

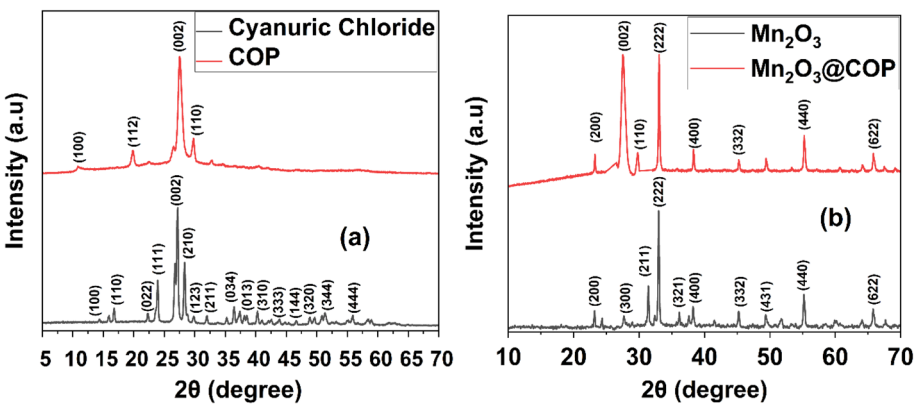

Fig. 5 XRD patterns of (a) cyanuric chloride, COP, and (b) Mn_2O_3, Mn_2O_3@COP.

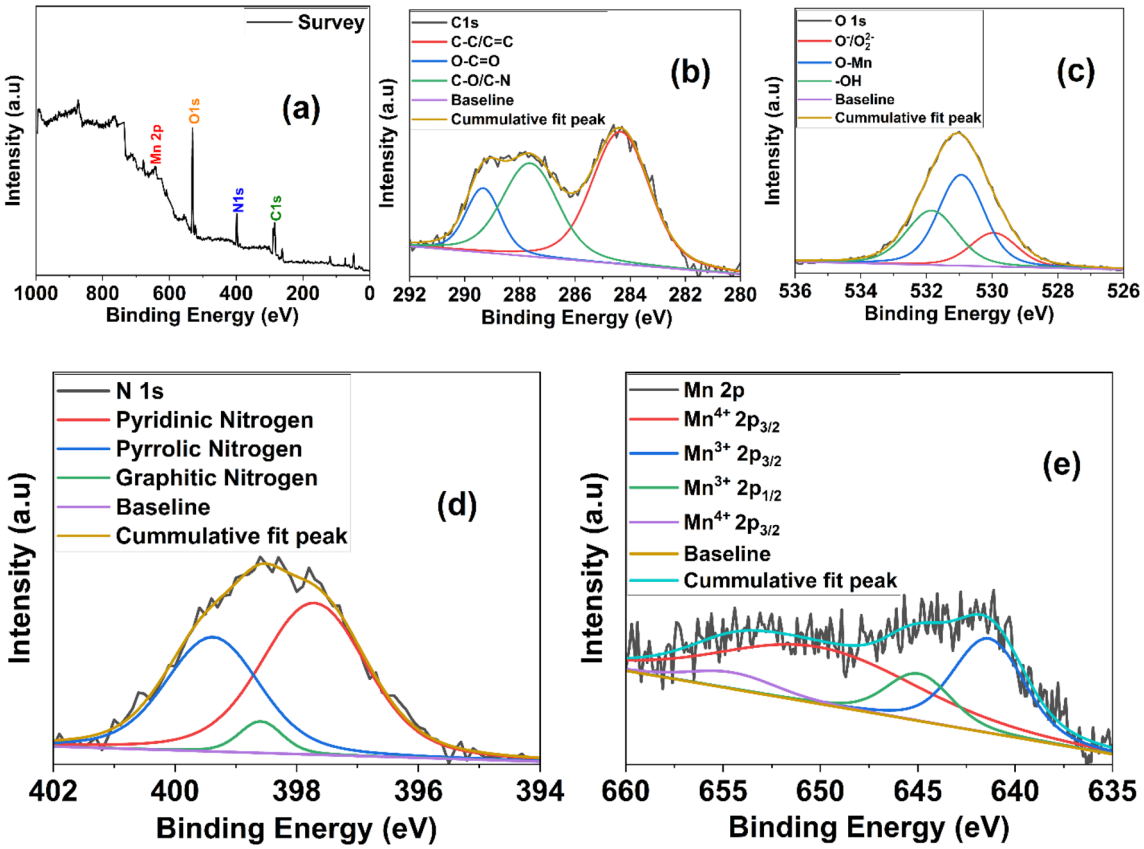

Fig. 6 XPS spectra of the Mn_2O_3@COP composite: (a) survey spectrum, (b) C1s, (c) O1s, (d) N1s, and (e) Mn 2p.

composite, which also match the structural characteristics observed in the solitary COP. Overall, the XRD results demonstrate the effective production of the Mn_2O_3@COP composite by confirming the presence of crystalline Mn_2O_3 domains embedded inside the amorphous COP framework.

3.3 XPS studies

High-resolution X-ray photoelectron spectroscopy (XPS) analysis of the Mn_2O_3@COP composite provides comprehensive insights into its surface chemistry and elemental composition (Fig. 6). The XPS survey spectrum of the Mn_2O_3@COP composite confirms the presence of Mn, O, N, and C. The C1s spectrum reveals multiple chemical environments of carbon. The dominant peak at ~284.6 eV corresponds to sp^2 hybridized carbon (C–C/C=C), which is indicative of the conjugated aromatic backbone of the COP and is likely composed of triazine and urea moieties. The second peak at ~286.0 eV is attributed to carbon bonded to electronegative atoms (C–O/C–N), suggesting the presence of nitrogen-rich functionalities and possible interactions with oxygen introduced during synthesis. The third peak, in the ~288.5–289.0 eV range, corresponds to oxidized carbon species such as carboxyl (O–C=O) or ester groups,[30] potentially arising from surface oxidation or chemisorbed oxygen linked to the Mn_2O_3 interface. These observations confirm the preservation of the COP framework and highlight its chemically active surface. The O1s spectrum further supported the complex surface chemistry of the composite. The main peak at ~531.2 eV is associated with lattice oxygen (O^{2-}) in Mn–O bonds,[31] confirming the presence of crystalline Mn_2O_3. A secondary peak at ~532.2 eV is assigned to surface hydroxyl groups or adsorbed water, which are common in hydrated or environmentally exposed materials.[32] The low-binding energy peak at ~529.9 eV is indicative of chemisorbed oxygen or oxygen vacancies[33] (O^-, O_2^{2-}), suggesting the presence of nonstoichiometric regions or defect sites within the Mn_2O_3 structure. This multiplicity of oxygen species points to a surface environment conducive to redox activity and ion transport, which are critical for electrochemical energy storage. The N1s spectrum revealed three distinct nitrogen species within the COP matrix. The peak at ~398.2 eV corresponds to pyridinic nitrogen,[34] which enhances the electron-donating capacity and supports redox behavior. The signal at ~399.5 eV is assigned to pyrrolic nitrogen,[35] which contributes to pseudocapacitance through proton-coupled electron transfer. The peak near ~400.6 eV corresponds to graphitic nitrogen,[36] which improves the electrical conductivity by integrating into the π-conjugated system.[37] The presence of these various nitrogen functionalities underscores the chemical richness of the COP framework and its potential role in facilitating both charge storage and transport. Finally, the Mn 2p spectrum reveals two sets of spin–orbit split peaks characteristic of the Mn^{3+} and Mn^{4+} oxidation states. The peaks at ~641.7 eV and ~653.4 eV are assigned to the Mn $2p_{3/2}$ and Mn $2p_{1/2}$ components of Mn^{3+}, respectively,[38] in agreement with

known values for Mn_2O_3. Moreover, the peaks at ~643.2 eV and ~654.9 eV correspond to the Mn $2p_{3/2}$ and $2p_{1/2}$ components of Mn^{4+}, which is consistent with MnO_2.[39] This mixed-valence state of manganese supports the redox-active nature of the composite, facilitating reversible faradaic processes. The coexistence of Mn^{3+}/Mn^{4+}, along with the rich surface chemistry of carbon, oxygen, and nitrogen species, suggests that the Mn_2O_3@COP composite possesses essential attributes for enhanced pseudocapacitive performance, including favorable charge transfer kinetics and high electrochemical activity, making it a promising candidate for advanced energy storage applications.

3.4 FE-SEM studies

SEM images revealed distinct morphological differences between the pristine COP (Fig. 7a) and the Mn_2O_3@COP composite (Fig. 7b). The COP results in a porous and loosely aggregated structure with irregular nanosheet-like features, characteristic of amorphous or weak crystalline polymer networks.[40] This morphology offers a high surface area, facilitating efficient electrolyte diffusion. Upon incorporation of Mn_2O_3, morphology transforms significantly, as observed in the formation of well-defined spherical particles distributed throughout the COP matrix.[41] These Mn_2O_3 particles, ranging from submicron to micron sizes, appear as dense clusters embedded within the polymer framework. This hierarchical architecture suggests successful nucleation and growth of Mn_2O_3 on the COP surface, likely due to strong physicochemical interactions. The composite structure synergistically combines the high surface area of the COP with the redox-active nature of Mn_2O_3, making it a promising candidate for supercapacitors. A particle size histogram (Fig. S1) was created *via* SEM image analysis to verify the nanoscale dispersion of Mn_2O_3 in the Mn_2O_3@COP composite. Uniform dispersion is shown by the size distribution plot's unimodal and very narrow distribution. The histogram data indicate that the average particle size of the Mn_2O_3@COP composite is approximately 106.75 nm, which is inside the nanodomain. The nanoscale size supports the excellent embedding and homogenous distribution of Mn_2O_3 particles inside the COP matrix, allowing for increased surface area exposure and possible electrochemical accessibility. Consequently, the size analysis and histogram support the assertion of the effective integration of Mn_2O_3 into the COP framework and its nanoscale dispersion (Fig. S2).

3.5 EDS studies

Fig. 8a shows the area where the EDS analysis was performed. The corresponding EDS spectrum (Fig. 8b) reveals clear peaks for carbon, nitrogen, oxygen, and manganese—elements that are consistent with both the COP structure and the Mn_2O_3 component. The composition table shows that manganese is present in the highest amount (42.97 wt%), followed by oxygen (33.19 wt%), carbon (17.26 wt%), and nitrogen (6.58 wt%). These values confirm that Mn_2O_3 is well incorporated into the polymer matrix. The presence of carbon and nitrogen indicates that the covalent organic polymer, which includes triazine and urea units, is retained in the final material. Overall, the EDS analysis confirmed the successful formation of the Mn_2O_3@COP composite.

3.6 BET and surface area studies

The nitrogen adsorption–desorption isotherms and pore size distribution profiles in Fig. 9 offer detailed insights into the textural characteristics of the pristine COP and the Mn_2O_3@COP composite. The isotherm of the COP (Fig. 9a) shows a classic type III pattern, which is commonly found in mesoporous materials that have slit-shaped pores.[42] As the relative pressure (p/p_o) increases, nitrogen uptake gradually increases, indicating a well-formed mesoporous structure that supports multilayer adsorption. A noticeable spike in nitrogen adsorption occurs near p/p_0 = 0.9–1.0, suggesting that capillary condensation takes place in larger mesopores or even macropores. This confirms the presence of a hierarchical pore system. The total amount of nitrogen adsorbed reached approximately 14 $cm^3\ g^{-1}$ STP, indicating a high surface area. The surface area of the COP was found to be 4.18 $m^2\ g^{-1}$. The inset graph reinforces these findings by displaying the pore size distribution calculated *via* the BJH method. The COP shows a narrow distribution, mostly concentrated between 2 and 3 nanometers, which confirms that mesopores are the primary feature of the material. A distinct peak at approximately 2.2 nm indicates a uniform mesoporous structure, which is beneficial for

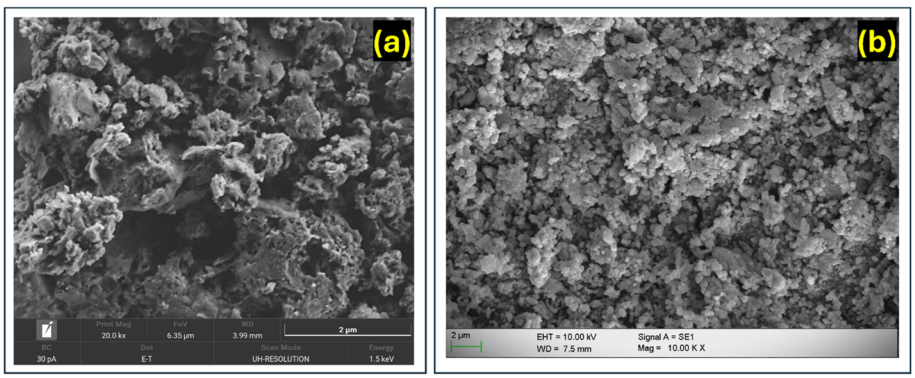

Fig. 7 FE-SEM images of (a) COP and (b) Mn_2O_3@COP.

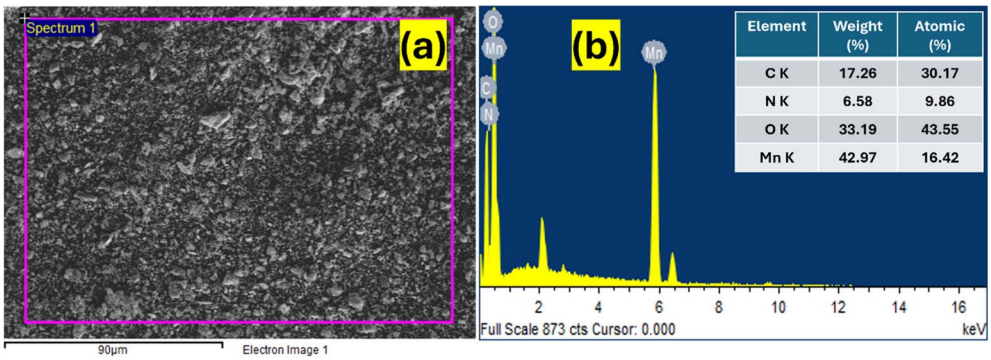

Fig. 8 (a) SEM image with EDS mapping region, (b) EDS spectrum with the inset of the elemental composition table of Mn_2O_3@COP.

efficient ion transport and better access to the electrolyte—key factors for effective charge storage applications. In contrast, the isotherm for the Mn_2O_3@COP composite shows a marked decrease in nitrogen uptake, with maximum adsorption reaching only approximately 5 $cm^3\ g^{-1}$ STP. The surface area of the Mn_2O_3@COP composite was found to be 0.11 $m^2\ g^{-1}$. This significant decline in the surface area is mainly due to the introduction of Mn_2O_3 nanoparticles into the COP structure. These metal oxide particles likely occupy some of the pore space or obstruct access to certain pores, leading to a decrease in both the accessible surface area and overall porosity. Nevertheless, the isothermal shape continues to indicate mesoporous features, although they are less prominent than those of the pristine COP. The hysteresis loop is still present but less distinct, and the sharp increase in adsorption at high relative pressures (p/p_0) continues to point to the existence of larger mesopores or voids between Mn_2O_3 particles that have clumped together. The inset graph of the pore size distribution again highlights mesopores, primarily in the 2–4 nm range, but with a reduced intensity and a wider spread than those of the pristine COP.

3.7 Electrochemical studies

3.7.1 Three-electrode system. The electrochemical performance of the Mn_2O_3@COP composite was thoroughly examined in a three-electrode configuration with 1 M H_2SO_4 as the electrolyte, and the findings are shown in Fig. 10. The CV curves have quasi rectangular profiles with minor redox peaks, indicating that the capacitive behavior is controlled by a mix of electric double-layer capacitance (EDLC) and pseudocapacitance. The triazine-based COP creates a highly porous and chemically stable matrix with several nitrogen-containing sites that aid in electron delocalization and charge storage *via* EDLC. Furthermore, the triazine units increase the wettability and chemical affinity with the aqueous electrolyte, allowing for efficient ion transport and quick charge propagation.[43] The addition of Mn_2O_3 nanoparticles into the COF matrix considerably enhances the pseudocapacitive component of charge storage. These Mn_2O_3 sites conduct reversible redox transformations (Mn^{3+}/Mn^{4+}) in the acidic environment of H_2SO_4, allowing faradaic charge storage beyond the contribution of the pure EDLC of the COF.[44] This synergy can be seen in the CV curves, where increasing scan rates result in greater current responsiveness while maintaining mild redox characteristics, indicating strong electrochemical reversibility and structural integrity under dynamic ion flow circumstances. The possible redox reactions involving Mn^{3+}/Mn^{4+} conversion are as follows:

$$Mn_2O_3 + H_2O \leftrightarrow 2MnO_2 + 2H^+ + 2e^-$$

$$Mn^{3+} \leftrightarrow Mn^{4+} + e^-$$

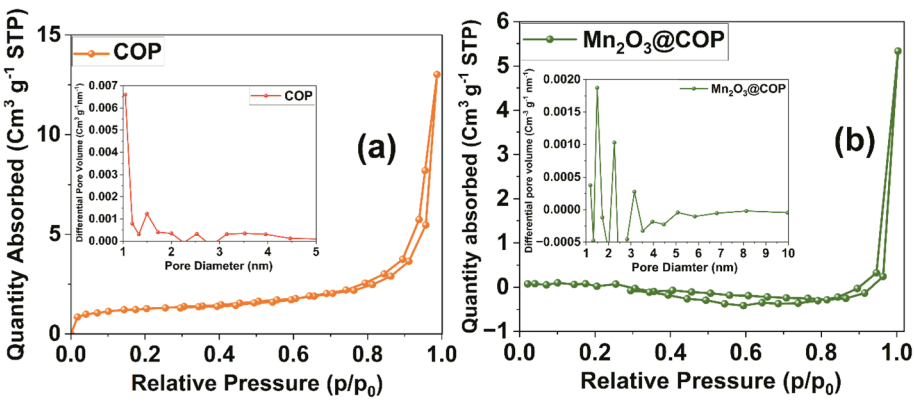

Fig. 9 N_2 adsorption/desorption isotherms of (a) COP and (b) Mn_2O_3@COP [inset: pore size distributions of COP and Mn_2O_3@COP.

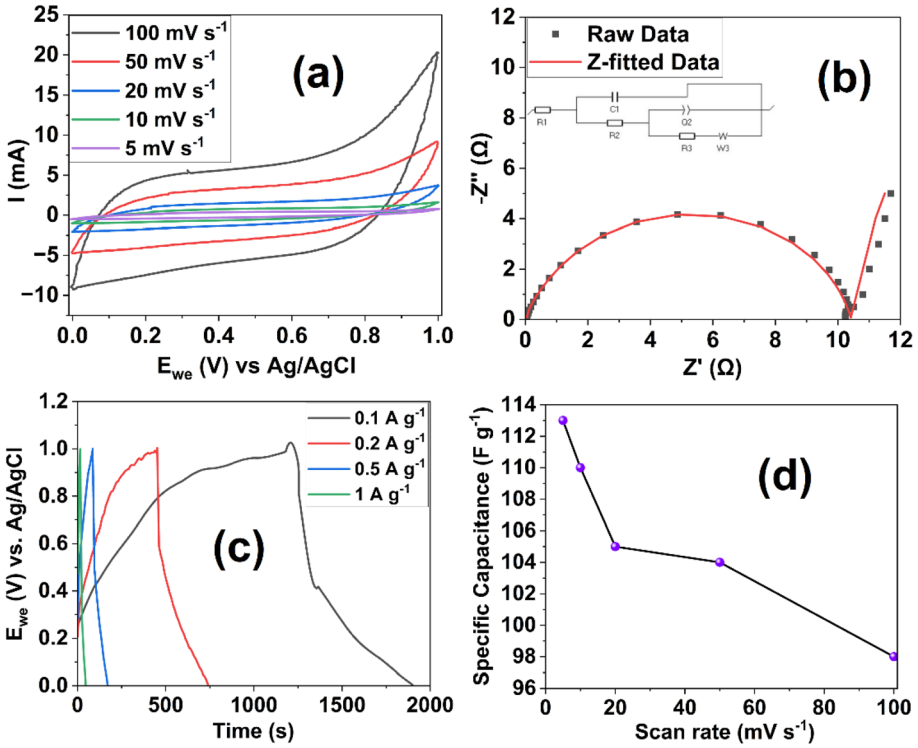

Fig. 10 Electrochemical behavior of the Mn_2O_3@COP composite in a three-electrode system using a 1 M H_2SO_4 electrolyte: (a) CV, (b) EIS, (c) GCD, and (d) specific capacitance at various current densities.

The Nyquist plot of the EIS data indicated a low equivalent series resistance (R_s), indicating good ionic conductivity enabled by the continuous COF network and the proton-rich environment of 1 M H_2SO_4. The moderate semicircle in the high-frequency region corresponds to the charge transfer resistance (R_{ct}), implying that the Mn redox processes have rather rapid kinetics. The linear Warburg zone in the low-frequency domain demonstrates advantageous ion diffusion behavior, which is most likely due to the hierarchical porosity and accessible surface area of the COF framework.[45] The GCD curves confirmed the composite's pseudocapacitive nature, exhibiting nonlinear potential–time profiles, particularly at lower current densities, that are consistent with the CV curves. The specific capacitance values determined from the GCD data indicate a decreasing trend with increasing current density (Fig. S3), from 69.1 F g^{-1} at 0.1 A g^{-1} to 30 F g^{-1} at 1 A g^{-1}, owing to restricted ion access to deep redox-active sites under high-rate circumstances. A similar pattern was found for the CV-derived capacitance values, which decreased from 113 F g^{-1} at 5 mV s^{-1} to 98 F g^{-1} at 100 mV s^{-1}, highlighting the diffusion-limited charge storage dynamics at higher scan rates. The energy density and power density values were found to be 9.6 Wh kg^{-1} and 500 W kg^{-1} at 0.1 A g^{-1}, respectively. The choice of 1 M H_2SO_4 as an electrolyte is crucial for improving the electrochemical performance. The strong ionic conductivity and proton availability of H_2SO_4 improve not only the electrolyte/electrode interface kinetics but also the redox activity of Mn_2O_3. The acidic medium stabilizes the Mn^{3+}/Mn^{4+} redox pair and increases the overall charge transfer efficiency, resulting in better capacitive behavior than that of neutral or alkaline media.[46] Overall, the triazine COF framework serves as an efficient conductive and porous support, while Mn_2O_3 offers redox activity, and the acidic environment promotes optimum ion dynamics, all of which contribute to the promising electrochemical properties of the Mn_2O_3@COF composite.

3.7.2 Supercapacitor application. Fig. 11 shows the electrochemical assessment of the Mn_2O_3@COP composite-based supercapacitor device, which was evaluated in a symmetric two-electrode configuration with a 1 M H_2SO_4 electrolyte. The CV curves displayed quasi rectangular behavior with small redox peaks at scan speeds ranging from 5 to 100 mV s^{-1}, indicating a mixture of EDLC and pseudocapacitance[47] similar to that of a three-electrode system. The EIS profile showed a typical Nyquist plot, with a tiny semicircle in the high-frequency area and a straight tail in the low-frequency region, suggesting low charge-transfer resistance and good ion diffusion properties[48] with an R_{ct} value of 190 Ω. The GCD curves at various current densities (0.2, 0.5, and 0.8 A g^{-1}) exhibited similar nonlinear potential–time profiles that were present in the three-electrode system, indicating good pseudocapacitive performance and great reversibility.[49] The specific capacitance decreased as the scan rate increased due to restricted ion diffusion (Fig. S4(a)). Similarly, there was a steady decrease in the specific capacitance with increasing current density (Fig. S4(b)), which is common in capacitive systems due to polarization effects. The specific capacitance values were found

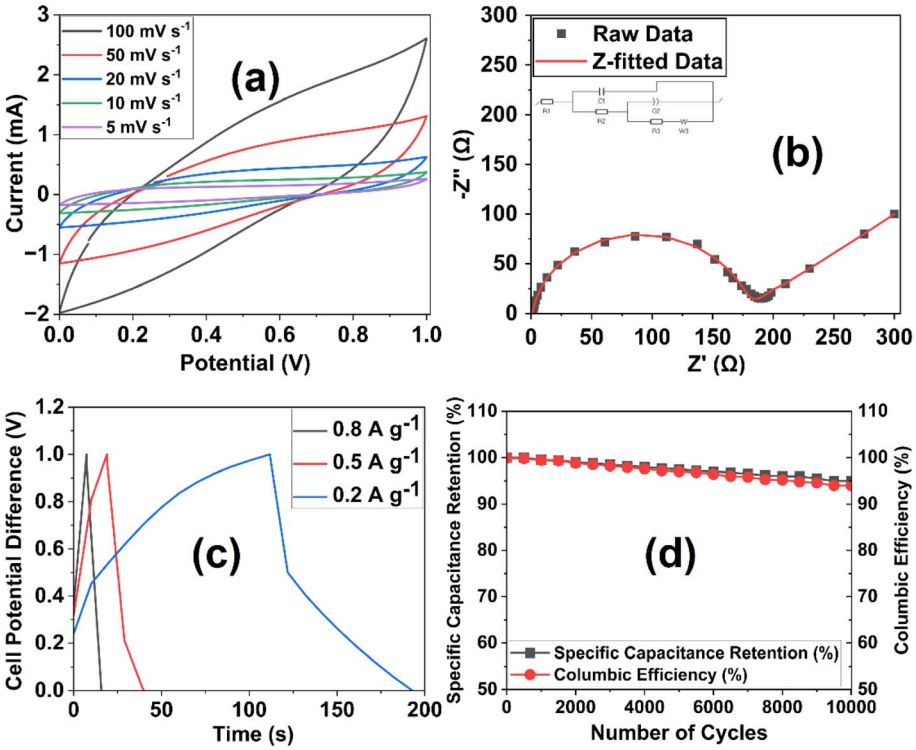

Fig. 11 Electrochemical behavior of a supercapacitor device with a Mn_2O_3@COP composite in a symmetric two-electrode system using a 1 M H_2SO_4 electrolyte: (a) CV, (b) EIS, (c) GCD, and (d) cycling stability.

to be 35 F g^{-1} at 5 mV s^{-1} and 16.2 F g^{-1} at 0.2 A g^{-1} from CV and GCD, respectively. Furthermore, the energy density and power density values were calculated to be 2.25 Wh kg^{-1} and 250 W kg^{-1}, respectively. The cycling stability test revealed excellent long-term durability, with a specific capacitance retention of 95% and a coulombic efficiency of 94% after 10 000 cycles at 0.5 A g^{-1}. This highlights the robustness of the electrode–electrolyte interface and the structural integrity of the composite. These findings highlight the effective electrochemical performance of Mn_2O_3@COP for supercapacitor applications.

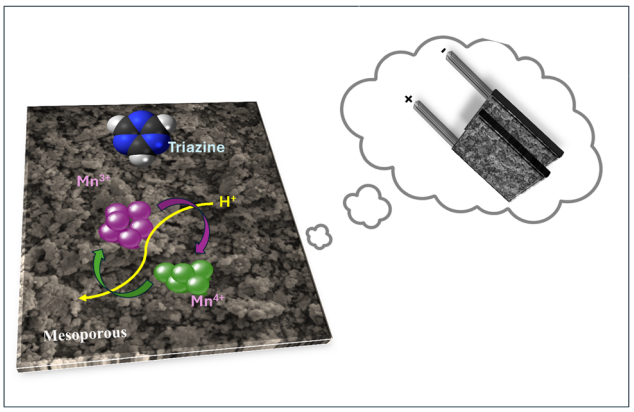

Fig. 12 Schematic illustration of the energy storage mechanism of the Mn_2O_3@COP composite along with the supercapacitor in the inset.

4 Mechanism

The electrochemical energy storage mechanism in the Mn_2O_3@COP composite is governed by a synergistic interplay between the EDLC and pseudocapacitance (Fig. 12). The triazine-based COP forms a porous, nitrogen-rich matrix that facilitates EDLC by offering abundant adsorption sites for electrolyte ions and promoting electron delocalization. This porous structure, along with enhanced surface wettability, allows for efficient ion diffusion and rapid charge–discharge cycles. The incorporation of Mn_2O_3 nanoparticles introduces redox-active sites that undergo reversible faradaic reactions, specifically Mn^{3+}/Mn^{4+} redox transitions, in an acidic 1 M H_2SO_4 environment. The H^+ ions actively participate in these redox transitions, enabling proton-coupled electron transfer reactions that enhance the pseudocapacitive behavior of the composite. These coupled processes are evident in the CV profiles, which exhibit quasi rectangular shapes with small redox humps. EIS confirmed efficient ion transport and low resistance within the system owing to both the high ionic conductivity of the acidic medium and the porous COP matrix. The GCD curves further support this hybrid mechanism, showing nonlinear potential–time behavior characteristic of pseudocapacitance. The performance decreases slightly at higher scan rates and current densities because of limited ion diffusion to deep redox-active sites, emphasizing the diffusion-controlled dynamics. Overall, the Mn_2O_3@COP composite achieves enhanced charge storage through a cooperative mechanism involving the EDLC from the COP, reversible redox reactions from Mn_2O_3, and crucial proton

Table 1 Specific capacitance performance of the Mn_2O_3@COP composite with previously reported materials

Sl. No.	Composite material	Specific capacitance (F g^{-1})	Reference
1	CFGCN-3 (triazine based)	147.22	50
2	Porous Mn_2O_3	102	51
3	Triazine-based CTF	151.3	52
4	IITR-COF-1	182.6	53
5	MnO_2-LCF-800	131.28	54
6	Mn_2O_3@COP	113	Present work
7	Al_2O_3@DHTA-COF composite	261.5	55
8	TPT@BDA-COF	92.6	56
9	Triazine-CTF/CNO	638	57
10	PDT-COF	104	58

participation from the H_2SO_4 electrolyte, all of which contribute to its superior supercapacitor performance.

The low electrochemical capacity observed in the present study can be attributed to factors such as poor electrode–electrolyte interfacial contact, limited intrinsic conductivity of the polymer, and restricted charge transport due to its disordered framework. These issues hinder effective ion diffusion and redox activity. To address these limitations, strategies such as incorporating aqueous-compatible conductive binders (*e.g.*, PEDOT:PSS, PVA, CMC), converting COPs into more crystalline COF structures, and integrating redox-active components such as metal oxides (NiO, V_2O_5) or carbon nanomaterials (graphene, CNTs) are proposed. This work highlights both the challenges and future directions for optimizing COP-based materials in energy storage applications (Table 1).

5 Conclusion

In summary, a triazine-based covalent organic polymer (COP) was effectively synthesized and integrated with Mn_2O_3 to construct a Mn_2O_3@COP composite electrode for high-performance supercapacitors. Comprehensive structural and surface investigations, including FTIR, XRD, SEM, EDS, BET, and XPS, indicated that the hierarchical composite was successfully formed. FTIR and XRD investigations confirmed the presence of Mn_2O_3 and the stability of the COP framework. SEM and EDS confirmed the homogeneous dispersion of Mn_2O_3 nanoparticles inside the porous matrix, whereas BET analysis revealed that the composite preserved mesoporous characteristics suitable for ion transport, despite a decreased surface area owing to Mn_2O_3 loading. XPS research revealed the existence of mixed-valence Mn^{3+}/Mn^{4+} species and nitrogen functionalities (pyridinic, pyrrolic, graphitic) in the COP, resulting in increased redox activity and charge transfer. Electrochemical investigations in three- and two-electrode configurations with a 1 M H_2SO_4 electrolyte revealed synergistic EDLC and pseudocapacitive behavior. The composite had a high specific capacitance of 113 F g^{-1} at 5 mV s^{-1} and 69.1 F g^{-1} at 0.1 A g^{-1}, an energy density of 9.6 Wh kg^{-1} and a power density of 500 W kg^{-1} at 0.1 A g^{-1}. The symmetric supercapacitor had a specific capacitance of 16.2 F g^{-1} and an energy density and power density of 2.25 Wh kg^{-1} and 250 W kg^{-1} at 0.2 A g^{-1}, respectively. Additionally, the device achieved 95% capacitance retention over 10 000 cycles. Thus, the Mn_2O_3@COP composite shows promise as a redox-active electrode material for long-lasting and efficient supercapacitor devices. In addition to its scientific merit, this work directly contributes to the United Nations Sustainable Development Goals: SDG 7 (Affordable and Clean Energy) through the development of high-performance energy storage materials; SDG 9 (Industry, Innovation and Infrastructure) by promoting advanced material innovation for sustainable technologies; and SDG 13 (Climate Action) by supporting low-carbon energy systems and facilitating the transition to clean energy infrastructure.

Conflicts of interest

There are no conflicts to declare.

Data availability

The data supporting this article have been included as part of the SI. See DOI: **https://doi.org/10.1039/d5ra04868k**.

References

1 L. Zhang, C. Jia, F. Bai, W. Wang, S. An, K. Zhao, *et al.*, A comprehensive review of the promising clean energy carrier: hydrogen production, transportation, storage, and utilization (HPTSU) technologies, *Fuel*, 2024, **355**, 129455.
2 P. K. Sahoo, N. Kumar, A. Jena, S. Mishra, C. P. Lee, S. Y. Lee, *et al.*, Recent progress in graphene and its derived hybrid materials for high-performance supercapacitor electrode applications, *RSC Adv.*, 2024, **14**(2), 1284–1303.
3 D. Yadav and S. K. Awasthi, A Pd NP-confined novel covalent organic polymer for catalytic applications, *New J. Chem.*, 2020, **44**(4), 1320–1325.
4 S. V. Sadavar, S. Lee and S. Park, Advancements in Asymmetric Supercapacitors: From Historical Milestones to Challenges and Future Directions, *Adv. Sci.*, 2024, **11**(34), 2403172.
5 Z. Hou, Q. Yang, H. Lu, Y. Li and Q. Zhao, Toward Superior Electrochemical Capacitance with Hierarchically Nanostructured Polypyrrole/MXene Hybrid Hydrogel

Modified by Lignosulfonate, *ACS Omega*, 2025, **10**(27), 29476–29487.

6 C. Chen, R. Yang, J. Zhu, W. Yao and Y. Tang, Superior Sodium Metal Anodes Enabled by 3D Hierarchical Metallic Scaffolds with Enhanced Sodiophilicity, *Adv. Sci.*, 2025, **12**(25), 2500756.

7 Z. Li, L. Gao, C. Zhang and F. Li, Copper incorporation induced oxygen vacancy MoO_3 anode and Zn dendrite inhibitor for high performance aqueous zinc ion batteries, *J. Energy Storage*, 2025, **119**, 116336.

8 Y. Liao, J. Li and A. Thomas, General Route to High Surface Area Covalent Organic Frameworks and Their Metal Oxide Composites as Magnetically Recoverable Adsorbents and for Energy Storage, *ACS Macro Lett.*, 2017, **6**(12), 1444–1450.

9 T. Li, W. D. Zhang, Y. Liu, Y. Li, C. Cheng, H. Zhu, *et al.*, A two-dimensional semiconducting covalent organic framework with nickel(ii) coordination for high capacitive performance, *J. Mater. Chem. A*, 2019, **7**(34), 19676–19681.

10 K. Kang, Z. Wu, M. Zhao, Z. Li, Y. Ma, J. Zhang, *et al.*, A nanostructured covalent organic framework with readily accessible triphenylstibine moieties for high-performance supercapacitors, *Chem. Commun.*, 2022, **58**(22), 3649–3652.

11 S. Jayakumar, P. C. Santhosh, M. M. Mohideen and A. V. Radhamani, A comprehensive review of metal oxides (RuO_2, Co_3O_4, MnO_2 and NiO) for supercapacitor applications and global market trends, *J. Alloys Compd.*, 2024, **976**, 173170.

12 S. A. Ansari, N. Parveen, H. M. Kotb and A. Alshoaibi, Hydrothermally derived three-dimensional porous hollow double-walled Mn_2O_3 nanocubes as superior electrode materials for supercapacitor applications, *Electrochim. Acta*, 2020, **355**, 136783.

13 W. Li, J. Shao, Q. Liu, X. Liu, X. Zhou and J. Hu, Facile synthesis of porous Mn_2O_3 nanocubics for high-rate supercapacitors, *Electrochim. Acta*, 2015, **157**, 108–114.

14 J. Xu, Y. Sun, M. Lu, L. Wang, J. Zhang, J. Qian, *et al.*, Fabrication of porous Mn_2O_3 microsheet arrays on nickel foam as high–rate electrodes for supercapacitors, *J. Alloys Compd.*, 2017, **717**, 108–115.

15 T. Singha, T. Kansaard, P. Jaiban, P. Suttiarporn, S. Wannapop, A. Phuruangrat, *et al.*, Highly improved electrochemical performance of $MnFe_2O_4$ electrode via Mn_2O_3 addition for supercapacitor applications, *Ceram. Int.*, 2025.

16 L. Zhao, S. Bi, J. Li, Y. Wen, H. Zhang, D. Zhang, *et al.*, Prussian blue analogues for advanced non-aqueous sodium ion batteries: redox mechanisms, key challenges and modification strategies, *Energy Storage Mater.*, 2025, **78**, 104256.

17 L. Tong, Y. Li, Y. Xu, J. Fang, C. Wen, Y. Zheng, *et al.*, A combined method for state-of-charge estimation for lithium-ion batteries based on IGWO-ASRCKF and ELM under various aging levels, *J. Energy Storage*, 2025, **124**, 116843.

18 L. Zhou, L. Xie, J. Dai, A. Jain, G. Chen and Y. Zhao, Orthogonal Test–Based Design and Optimization of a Li-Ion Battery Thermal Management System With a Liquid-Cooled Reverse Parallel Structure and Inlaid Fins, *Asia-Pac. J. Chem. Eng.*, 2025, e70056.

19 C. j. Wang, Y. Zhu, T. Zhang, J. Tian, F. Gao, Y. Zhao, *et al.*, Competition between discharge reaction and side reaction for anode's lithium during internal short circuit in lithium-ion batteries, *J. Cleaner Prod.*, 2024, **470**, 143280.

20 L. Zhu, Y. Song, H. Chen, M. Wang, Z. Liu, X. Wei, *et al.*, Optimization of power generation and sewage treatment in stacked pulsating gas-liquid-solid circulating fluidized bed microbial fuel cell using response surface methodology, *Int. J. Hydrogen Energy*, 2025, **101**, 161–172.

21 Y. Bian, L. Xie, L. Ma and C. Cui, A novel two-stage energy sharing model for data center cluster considering integrated demand response of multiple loads, *Appl. Energy*, 2025, **384**, 125454.

22 S. Verma, G. Kumar, A. Ansari, R. I. Kureshy and N. u. H. Khan, A nitrogen rich polymer as an organo-catalyst for cycloaddition of CO_2 to epoxides and its application for the synthesis of polyurethane, *Sustainable Energy Fuels*, 2017, **1**(7), 1620–1629.

23 W. Tariq, M. Pudukudy, Y. Liu, S. Li, C. Zhang, H. A. Ali, *et al.*, Nitrogen-rich covalent-organic-framework as a recyclable heterogenous catalyst for the efficient cycloaddition of carbon dioxide with epoxides, *Sep. Purif. Technol.*, 2025, **353**, 128361.

24 V. Timón, B. Maté, V. J. Herrero and I. Tanarro, Infrared spectra of amorphous and crystalline urea ices, *Phys. Chem. Chem. Phys.*, 2021, **23**(39), 22344–22351.

25 M. Wu, J. M. Yan, X. W. Zhang, M. Zhao and Q. Jiang, Ag_2O modified g-C_3N_4 for highly efficient photocatalytic hydrogen generation under visible light irradiation, *J. Mater. Chem. A*, 2015, **3**(30), 15710–15714.

26 G. Munir, H. E. A. Mohamed, K. Hkiri, S. Ghotekar and M. Maaza, Phyto-mediated fabrication of Mn_2O_3 nanoparticles using hyphaene thebaica fruit extract as a promising photocatalyst for MB dye degradation, *Inorg. Chem. Commun.*, 2024, **167**, 112695.

27 M. Xie, W. Wei, Z. Jiang, Y. Xu and J. Xie, Carbon nitride nanowires/nanofibers: a novel template-free synthesis from a cyanuric chloride–melamine precursor towards enhanced adsorption and visible-light photocatalytic performance, *Ceram. Int.*, 2016, **42**(3), 4158–4170.

28 D. Yadav and S. K. Awasthi, A Pd confined hierarchically conjugated covalent organic polymer for hydrogenation of nitroaromatics: catalysis, kinetics, thermodynamics and mechanism, *Green Chem.*, 2020, **22**(13), 4295–4303.

29 A. Umar, I. Jung, A. A. Ibrahim, M. S. Akhtar, S. A. Kumar, M. A. M. Alhamami, *et al.*, Porous Mn_2O_3 nanorods-based electrode for high-performance electrochemical supercapacitor, *J. Energy Storage*, 2024, **81**, 110305.

30 Q. Zeng, Y. Li, K. H. Wu, N. Huang, S. Dalapati, B. J. Su, *et al.*, Long-chain solid organic polysulfide cathode for high-capacity secondary lithium batteries, *Energy Storage Mater.*, 2018, **12**, 30–36.

31 E. Symianakis, D. Malko, E. Ahmad, A. S. Mamede, J. F. Paul, N. Harrison, *et al.*, Electrochemical Characterization and Quantified Surface Termination Obtained by Low Energy

Ion Scattering and X-ray Photoelectron Spectroscopy of Orthorhombic and Rhombohedral $LaMnO_3$ Powders, *J. Phys. Chem. C*, 2015, **119**(22), 12209–12217.

32 D. V. Sivkov, O. V. Petrova, S. V. Nekipelov, A. S. Vinogradov, R. N. Skandakov, K. A. Bakina, *et al.*, Quantitative Characterization of Oxygen-Containing Groups on the Surface of Carbon Materials: XPS and NEXAFS Study, *Appl. Sci.*, 2022, **12**(15), 7744.

33 T. Li, S. Abuelgasim, W. Wang, Y. Xiao, C. Liu, Y. Ying, *et al.*, Enhanced soot oxidation by oxygen vacancies via K^+ doped $CuFe_2O_4$ spinel catalysts, *Int. J. Energy Res.*, 2022, **46**(11), 15376–15386.

34 C. Alegre, D. Sebastián, M. J. Lázaro, M. Girolamo, A. S. Aricò and V. Baglio, Influence of Nitrogen and Sulfur Doping of Carbon Xerogels on the Performance and Stability of Counter Electrodes in Dye Sensitized Solar Cells, *Catalysts*, 2022, **12**(3), 264.

35 L. M. Ombaka, P. G. Ndungu and V. O. Nyamori, Pyrrolic nitrogen-doped carbon nanotubes: physicochemical properties, interactions with Pd and their role in the selective hydrogenation of nitrobenzophenone, *RSC Adv.*, 2015, **5**(1), 109–122.

36 W. J. Gammon, O. Kraft, A. C. Reilly and B. C. Holloway, Experimental comparison of N(1s) X-ray photoelectron spectroscopy binding energies of hard and elastic amorphous carbon nitride films with reference organic compounds, *Carbon*, 2003, **41**(10), 1917–1923.

37 P. Puthiaraj and K. Pitchumani, Palladium nanoparticles supported on triazine functionalised mesoporous covalent organic polymers as efficient catalysts for Mizoroki–Heck cross coupling reaction, *Green Chem.*, 2014, **16**(9), 4223–4233.

38 S. Bhowmick, M. K. Mohanta and M. Qureshi, Transcription methodology for rationally designed morphological complex metal oxides: a versatile strategy for improved electrocatalysis, *Sustainable Energy Fuels*, 2021, **5**(24), 6392–6405.

39 M. He, Z. Turup, X. Jin and F. Chen, Ag nanoparticle-loaded to MnO_2 with rich oxygen vacancies and Mn^{3+} for the synergistically enhanced oxygen reduction reaction, *Int. J. Hydrogen Energy*, 2023, **48**(66), 25770–25782.

40 D. Yadav and S. K. Awasthi, A Pd confined hierarchically conjugated covalent organic polymer for hydrogenation of nitroaromatics: catalysis, kinetics, thermodynamics and mechanism, *Green Chem.*, 2020, **22**(13), 4295–4303.

41 A. K. M. A. Ullah, A. K. M. F. Kibria, M. Akter, M. N. I. Khan, M. A. Maksud, R. A. Jahan, *et al.*, Synthesis of Mn_3O_4 nanoparticles via a facile gel formation route and study of their phase and structural transformation with distinct surface morphology upon heat treatment, *J. Saudi Chem. Soc.*, 2017, **21**(7), 830–836.

42 R. L. Wang, D. P. Li, L. J. Wang, X. Zhang, Z. Y. Zhou, J. L. Mu, *et al.*, The preparation of new covalent organic framework embedded with silver nanoparticles and its applications in degradation of organic pollutants from wastewater, *Dalton Trans.*, 2019, **48**(3), 1051–1059.

43 P. R. R. Divya, S. Ali, M. E. Ali, S. Kalla, R. K. Pandey, *et al.*, An electron rich triazine-based covalent organic framework as an aqueous electrolyte symmetric supercapacitor, *Chem. Commun.*, 2025, **61**(43), 7831–7834.

44 S. Nijjer, J. Thonstad and G. M. Haarberg, Oxidation of manganese(II) and reduction of manganese dioxide in sulphuric acid, *Electrochim. Acta*, 2000, **46**(2–3), 395–399.

45 F. Gong, S. Lu, L. Peng, J. Zhou, J. Kong, D. Jia, *et al.*, Hierarchical Mn_2O_3 Microspheres In-Situ Coated with Carbon for Supercapacitors with Highly Enhanced Performances, *Nanomaterials*, 2017, **7**(12), 409.

46 P. Adoor, S. S. Hegde, B. R. Bhat, S. D. George and R. Yeenduguli, Electrochemical performance and structural evolution of spray pyrolyzed Mn_3O_4 thin films in different aqueous electrolytes: effect of anions and cations, *RSC Adv.*, 2024, **14**(41), 29748–29762.

47 M. C. Lin, S. W. Kuo and M. G. Mohamed, High-performance anthracene-linked covalent triazine frameworks with dual functions for CO_2 capture and supercapacitor applications, *Mater. Adv.*, 2024, **5**(15), 6222–6233.

48 N. Deka, R. Patidar, S. Kasthuri, N. Venkatramaiah and G. K. Dutta, Triazine based polyimide framework derived N-doped porous carbons: a study of their capacitive behaviour in aqueous acidic electrolyte, *Mater. Chem. Front.*, 2019, **3**(4), 680–689.

49 X. Hao, J. Wang, B. Ding, Z. Chang, Y. Wang, H. Dou, *et al.*, Nitrogen-Doped Porous Carbon Nanospheres from Natural Sepia Ink: Easy Preparation and Extraordinary Capacitive Performance, *ChemNanoMat*, 2017, **3**(12), 895–901.

50 C. Harak, V. Kadam, R. Gavhane, S. Balgude, A. Rakshe, N. Brahmankar, *et al.*, Enhanced supercapacitor performance of a Cu-Fe_2O_3/g-C_3N_4 composite material: synthesis, characterization, and electrochemical analysis, *RSC Adv.*, 2024, **14**(7), 4917–4929.

51 D. Shao, X. Li, M. Yang, J. Li, R. Chen, X. Zheng, *et al.*, Synthesis of porous Mn_2O_3 architecture for supercapacitor electrode application, *Colloids Surf., A*, 2023, **658**, 130532.

52 X. Chen, R. Paul and L. Dai, Carbon-based supercapacitors for efficient energy storage, *Natl. Sci. Rev.*, 2017, **4**(3), 453–489.

53 Y. Kumar, I. Ahmad, A. Rawat, R. K. Pandey, P. Mohanty and R. Pandey, Flexible Linker-Based Triazine-Functionalized 2D Covalent Organic Frameworks for Supercapacitor and Gas Sorption Applications, *ACS Appl. Mater. Interfaces*, 2024, **16**(9), 11605–11616.

54 C. Guo, H. Ma, Q. Zhang, M. Li, H. Jiang, C. Chen, *et al.*, Nano MnO_2 Radially Grown on Lignin-Based Carbon Fiber by One-Step Solution Reaction for Supercapacitors with High Performance, *Nanomaterials*, 2020, **10**(3), 594.

55 L. Liu, D. Cui, S. Zhang, W. Xie, C. Yao, N. Xu, *et al.*, Triazine covalent organic framework (COF)/θ-Al_2O_3 composites for supercapacitor application, *Dalton Trans.*, 2023, **52**(18), 6138–6145.

56 I. Ahmad, O. Singh, J. Ahmed, A. S. M. Priyanka, C. Bharti, *et al.*, Triazine-Functionalized Nitrogen-Rich Covalent Organic Framework as an Electrode Material for Aqueous Symmetric Supercapacitor, *Chem.–Asian J.*, 2025, **20**(5), e202401149.

57 A. Hryniewicka, J. Breczko, G. Siemiaszko, A. N. Papathanassiou, K. Góra-Marek, K. A. Tarach, *et al.*, Three-dimensional organization of pyrrolo[3,2-*b*]pyrrole-based triazine framework using nanostructural spherical carbon: enhancing electrochemical performance of materials for supercapacitors, *Sci. Rep.*, 2023, **13**(1), 10737.

58 S. Halder and C. Chakraborty, Triazine-Based Two-Dimensional Porous Covalent Organic Framework for Efficient Electrode Materials for Electrocatalytic Hydrogen Generation and Hybrid Supercapacitors, *ACS Appl. Eng. Mater.*, 2023, **1**(7), 1799–1808.